3-5-2021

Evolving Tides Aggravate Nuisance Flooding Along the U.S. Coastline.

Sida Li
University of Chinese Academy of Sciences

Thomas Wahl
University of Central Florida

Stefan A. Talke
California Polytechnic State University, talke@pdx.edu

David A. Jay
Portland State University, djay@pdx.edu

Philip M. Orton
Stevens Institute of Technology

See next page for additional authors

Citation Details

Li, S., Wahl, T., Talke, S. A., Jay, D. A., Orton, P. M., Liang, X., Wang, G., & Liu, L. (2021). Evolving tides aggravate nuisance flooding along the U.S. coastline. *Science Advances*, *7*(10), eabe2412. https://doi.org/10.1126/sciadv.abe2412

JGR Oceans

RESEARCH ARTICLE
10.1029/2019JC015286

Key Points:
- An idealized model shows that channel deepening increases surge amplitude and moves the location of maximum change in surge landward
- The damping in storm surge varies spatially and depends on surge time scale, amplitude, asymmetry, and timing relative to tides
- The largest amplification in surge due to channel deepening occurs in strongly frictional estuaries for large amplitude fast moving events

Supporting Information:
- Supporting Information S1

Correspondence to:
R. Familkhalili,
rfa2@pdx.edu

Citation:
Familkhalili, R., Talke, S. A., & Jay, D. A. (2020). Tide-storm surge interactions in highly altered estuaries: How channel deepening increases surge vulnerability. *Journal of Geophysical Research: Oceans*, *125*, e2019JC015286. https://doi.org/10.1029/2019JC015286

Received 15 MAY 2019
Accepted 2 MAR 2020
Accepted article online 10 MAR 2020

Tide-Storm Surge Interactions in Highly Altered Estuaries: How Channel Deepening Increases Surge Vulnerability

R. Familkhalili[1], S. A. Talke[2], and D. A. Jay[1]

[1]Department of Civil and Environmental Engineering, Portland State University, Portland, OR, USA, [2]Department of Civil and Environmental Engineering, California Polytechnic State University, San Luis Obispo, CA, USA

Abstract We develop idealized analytical and numerical models to study how storm surge amplitudes vary within frictional, weakly convergent, nonreflective estuaries. Friction is treated using Chebyshev polynomials. Storm surge is represented as the sum of two sinusoidal components, and a third constituent represents the semidiurnal tide (D_2). An empirical fit of storm surge shows that two sinusoidal components adequately represent storm surge above a baseline value ($R^2 = 0.97$). We find that the spatial transformation of surge amplitudes depends on the depth of the estuary, and characteristics of the surge wave including time scale, amplitude, asymmetry, and surge-tide relative phase. Analytical model results indicate that surge amplitude decays more slowly (larger *e*-folding) in a deeper channel for all surge time scales (12–72 hr). Deepening of an estuary results in larger surge amplitudes. Sensitivity studies show that surges with larger primary amplitudes (or shorter time scales) damp faster than those with smaller amplitudes (or larger time scales). Moreover, results imply that there is a location with maximum sensitivity to altered depth, offshore surge amplitude, and time scale and that the location of observed maximum change in surge amplitude along an estuary of simple form moves upstream when depth is increased. Further, the relative phase of surge to tide and surge asymmetry can change the spatial location of maximum change in surge. The largest change due to increased depth occurs for a large surge with a short time scale. The results suggest that both sea level rise and channel deepening may also alter surge amplitudes.

Plain Language Summary Many estuaries around the world are heavily altered from their natural state. Wetlands have been reclaimed, and shipping channels widened and deepened to accommodate large container ships. The effects on storm surge and flood risk are just beginning to be explored. In this paper we employ a theoretical approach to understand how the characteristics of a storm surge—such as how fast it is moving, how big it is, and whether it happens on flood or ebb tide—change how it behaves in an estuary. Our results show that storm surge generally gets larger when channels are dredged and deepened; the largest amplification is observed for fast-moving storms with a short time scale, within estuaries that are highly frictional. Other characteristics—such as the timing relative to the tide and the shape of the estuary—also impact the amplitude and the amount of sensitivity to changing conditions. We find that channel deepening effects are negligible at the coast and far upstream. In between, a region of maximum sensitivity to dredging occurs. Thus, changes in flood risk due to channel deepening and sea level rise can be spatially variable, even within a single estuary.

1. Introduction

As global sea level rises, there is increasing concern that increased depth may amplify tide amplitudes and alter tidal phases at the estuary scale (Cai et al., 2012; Holleman & Stacey, 2014; Lee et al., 2017; Talke & Jay, 2020). Similarly, there is a growing recognition that local bathymetric changes such as channel deepening can significantly alter tide, circulation, and transport patterns within estuaries (e.g., Chant et al., 2018; Chernetsky et al., 2010; de Jonge et al., 2014; Jay et al., 2011; van Rijn et al., 2018). Since coastal storm surge caused by wind occurs over a similar time scale and with similar amplitude as a tide wave, changes in estuary bathymetry also affect surge magnitudes and flood risk (e.g., Orton et al., 2015; Talke et al., 2014). Most dramatically, a doubling of channel depth in the Cape Fear Estuary (NC) since 1880s resulted in a doubling of tide range and a large (1.8 m) increase in the modeled surge due to the worst-case scenario hurricane

(Familkhalili & Talke, 2016). In the Hudson River, tides at Albany (NY) have approximately doubled since 1930 due to dredging (Ralston et al., 2019; Schureman, 1934) and were shown through modeling to produce a significant increase in storm surge magnitudes (Ralston et al., 2019). On the other hand, the tide range in New York harbor has changed only slightly since the midnineteenth century (Talke et al., 2014), and modeling suggested that historical channel deepening only altered tide range within the harbor by 0.1 m (~7%) (Ralston et al., 2019).

Hence, longwave amplitudes at some locations within estuaries appear to be quite sensitive to changing conditions, while others seem relatively impervious to change. Since altered tide and storm surges have implications for flood hazard, a better understanding of how and why storm surge magnitudes vary within an estuary has obvious practical importance. Here, we use a well-known analytical approach that has previously been used for tides (e.g., Jay, 1991; Jay & Flinchem, 1997) and apply the tools and lessons of tide analysis to gain new insights into how and why storm surge magnitudes change within an estuary.

Storm surge is a meteorologically forced longwave generated by storm winds and interacts with storm waves and astronomical tides in coastal regions to produce flood waters (e.g., McRobie et al., 2005; Wolf & Flather, 2005). The magnitude and time scale of a storm surge within an estuary depend on the intensity, size, and path of the storm (Orton et al., 2016; Peng et al., 2004; Rego & Li, 2010; Xia et al., 2008), the geometric properties of the estuary (Familkhalili & Talke, 2016; Orton et al., 2015), and nonlinear frictional interactions with other hydrodynamic processes, including river flow, astronomical tides, and wind waves (Maskell et al., 2013). At the same time, the storm surge modifies the hydrodynamic processes with which it interacts, for example, shifting the phase (Horsburgh & Wilson, 2007) and altering the amplitude (Arns et al., 2017) of the tide wave. Quantifying such effects, however, remains challenging and is typically assessed by simulating storm surge in a numerical model that is run with and without tides (e.g., Lyddon et al., 2018; Shen et al., 2006). The difference between the modeled storm surge waves is then attributed to nonlinear tide-surge interaction. However, this approach cannot determine how much each tide (or surge) wave has been altered.

We suggest that new insights can be gained into the behavior of surge in estuaries—and its nonlinear interaction with tides—by approximating its behavior using analytical models developed for tides. Tides and surge have similar time scales, are longwaves described by the shallow-water equations, and may, therefore, be amenable to similar solution methodologies. Extensive studies have analytically investigated the influence of geometrical variations of estuaries (e.g., depth, cross-sectional area, and convergence) on tidal propagation (e.g., Dronkers, 1964; Friedrichs & Aubrey, 1994; Godin, 1999; Jay, 1991; Kukulka & Jay, 2003; Lanzoni & Seminara, 1998). Moreover, a subset of analytical models have investigated the interaction between two or three tidal constituents or between tides and river flow (e.g., Giese & Jay, 1989; Godin, 1999; Jay & Flinchem, 1997; Toffolon & Savenije, 2011). Here, we argue that insights into tide-surge interactions can be obtained by using an analytical model with three sinusoidal waves. Two of the sinusoidal waves simulate the effects of surge and the third models the semidiurnal (D_2) tidal frequency.

If surge can be approximated as the sum of sinusoidal waves, the tidal literature can guide analysis of surge propagation within estuaries and help explain the effects of changing geometry (such as depth). Tidal theory explains wave dynamics in estuaries as a balance between inertia (acceleration and deceleration effects), amplification (due to the convergence), damping (due to bottom friction), and energy exchange between frequencies. Tidal amplitudes decrease in the upstream direction when frictional effects dominate over the funneling effect caused by decreasing width; by contrast, strong convergence can produce increasing amplitude when friction is relatively weak. Therefore, changing the balance between bed friction, convergence, and river flow helps determine whether tidal amplitudes reduce, increase, or remain constant along a convergent estuary (e.g., Jay, 1991; Talke & Jay, 2020).

In this paper, we develop an analytical model of surge based on previous multiconstituent models (e.g., Buschman et al., 2009; Giese & Jay, 1989; Jay & Flinchem, 1997; Parker, 1991). We first use empirical data to justify the use of two sinusoidal components to model surge effects and quantify the range of time scales and amplitudes of surge that is typically observed in a representative coastal plain estuary on the U.S. East Coast, the Delaware Bay. Since a significant portion of Delaware Bay is funnel shaped, and the increase in tide magnitudes due to channel dredging is well established (DiLorenzo et al., 1993), our modeling approach is well suited for understanding whether surge amplitudes have changed over time due to altered

bathymetry. Next, we develop our analytical model by semilinearizing friction using the Godin (1991a, 1999) approach, which involves using Chebyshev polynomials and trigonometric identities to derive terms with combinations of frequencies. We employ a multisection approach and determine the friction term iteratively to account for along-channel variation of width and effective friction. To show that results are reasonable, the analytical model is then validated against an idealized numerical model that is run using the same configuration. The resulting analytical model is fast, simple, and enables the quick sampling of a large parameter space. We demonstrate the explanatory power of the model by showing how important parameters —such as the estuary depth, the surge amplitude and time scale, and the relative phasing of surge with the tide—affect the spatial damping (or amplification) of the surge wave.

2. Methods

2.1. Analytical Model

Computer simulations are widely used to model storm surge in specific coastal areas (e.g., Orton et al., 2012) or in idealized geometry (e.g., Familkhalili & Talke, 2016), but analytical models are transparent, quick to run, and enable the investigation of both individual parameters and their nonlinear interaction (e.g., Chernetsky et al., 2010). Using these models, the analytical effects of changing parameters (e.g., depth) can be found for different types of systems and different boundary forcing.

Here we outline the theoretical basis of a three-component wave model, closely following the approach of Jay (1991) and Giese and Jay (1989). One-dimensional longwave propagation along a channel in an idealized estuary is described by the cross-sectionally integrated equations for conservation of mass and momentum (e.g., Jay, 1991):

$$\underbrace{\frac{\partial Q}{\partial t}}_{\substack{\text{Local}\\ \text{acceleration}}} + \underbrace{\frac{\partial}{\partial x}\left(\frac{Q^2}{A}\right)}_{\substack{\text{Convective}\\ \text{acceleration}}} + \underbrace{gA\frac{\partial \xi}{\partial x}}_{\substack{\text{Pressure}\\ \text{gradient}}} + \underbrace{bT}_{\text{Friction}} = 0 \tag{1}$$

$$\underbrace{\frac{\partial Q}{\partial x}}_{\substack{\text{Water}\\ \text{transport}}} + \underbrace{b\frac{\partial \xi}{\partial t}}_{\substack{\text{Temporal water}\\ \text{surface elevation}}} = 0 \tag{2}$$

where Q is cross-sectionally integrated flow, t is time, x is the longitudinal coordinate measured in landward direction ($x = 0$ at the mouth, see Figure 1), b is width, g is acceleration due to gravity, A is channel cross section, ξ is elevation of the tide water level, and T is the bed stress divided by water density. Cross-sectionally integrated flow (Q) is equal to (Q_R+Q_T) (i.e., the summation of river flow Q_R, invariant in time and space, and tidal transport $Q_{T(x,t)}$). The conceptual plan of the model of tidal wave is shown in Figure 1. We consider a constant depth and assume that the width of the channel is an exponentially decreasing function of the longitudinal coordinate x, which approximates a typical midlatitude coastal plain estuary:

$$b_{(x)} = B_c + (B_0 - B_c)e^{\left(-\frac{x}{L_e}\right)} \tag{3}$$

where $B_0$is the width at the estuary mouth, B_c is a constant that models the river width in the landward part of the domain, and $L_e$is the convergence length scale (i.e., the length over which the width decreases by a factor of e).

We assume that the tidal amplitude to depth ratio $\left(\frac{\xi}{h}\right)$ is small and river flow (Q_R) is constant, since variability from a storm-driven river freshet typically occurs a day or more after the storm (e.g., Divoky et al., 2005), depending on watershed characteristics. Subtracting the time derivative of the momentum equation (equation 1) from the spatial derivative of the continuity equation (equation 2), and using $Q = Q_R + Q_T$, results in a wave equation that describes the wave propagation along a channel without tidal flats (Kukulka & Jay, 2003):

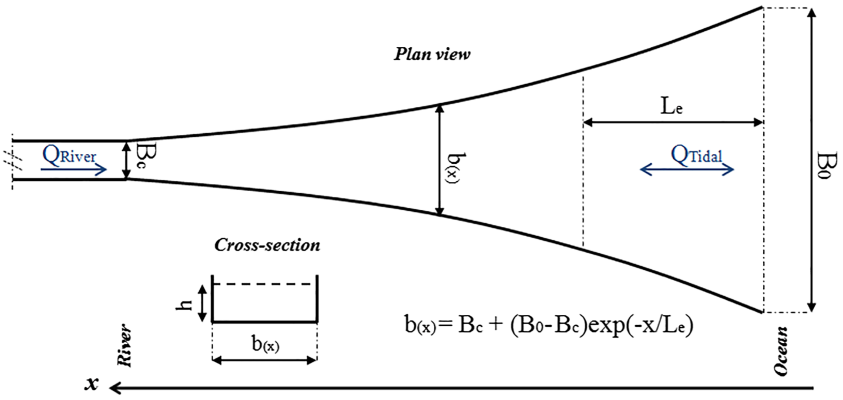

Figure 1. The conceptual plan view and cross-section area of the idealized model used in the study.

$$\underbrace{\frac{\partial^2 Q_T}{\partial x^2}}_{\text{Pressure gradient}} - \underbrace{\frac{1}{b}\frac{\partial b}{\partial x}\frac{\partial Q_T}{\partial x}}_{\text{Pressure gradient and convergence}} \underbrace{-2\frac{1}{gh}U_R\frac{\partial^2 Q_T}{\partial x \partial t} + 2\frac{1}{gh}U_R\frac{1}{A}\frac{\partial A}{\partial x}\frac{\partial Q_T}{\partial t}}_{\text{Convective acceleration}} - \underbrace{\frac{1}{gh}\frac{\partial^2 Q_T}{\partial t^2}}_{\text{Local acceleration}} \underbrace{-\frac{b}{gh}\frac{\partial T}{\partial t}}_{\text{Friction}} = 0 \quad (4)$$

where h is the depth and U_R is the river flow velocity. The nonlinear frictional interaction is represented by $T = \frac{\tau}{\rho} = C_d|u|u$, where the velocity u is the summation of river flow U_R and the tidal flow U_T, and $C_d$is the drag coefficient. To compare the results of the analytical model with an idealized numerical model (see section 2.2), the drag coefficient is converted to a Chezy coefficient $C_h(\frac{m^{1/2}}{s})$ using $C_d = {}^{g}/_{C_h{}^2}$. Scaling shows that convective acceleration is small or negligible in our smooth geometry. An analytical solution for equation 4 is possible after assuming a sinusoidal solution and linearizing the quadratic friction term (see the supporting information for details).

Although the width of the continental shelf and the propagation speed, width, and storm-track influence storm surge time scale and magnitudes (e.g., Orton et al., 2016), we neglect such complexity. Instead, we consider coastal-generated surge as a boundary condition and investigate how surge behaves in the estuary, once generated. We also neglect the effect of Coriolis acceleration and other factors that produce cross-channel tidal variability, since empirical and modeling observations (e.g., in Delaware Bay; see Lee et al., 2017) show that cross-sectional tidal amplitude variation is small in large estuaries and negligible in the narrow (<~10 km) reaches we consider. Furthermore, we assume no overland flooding and consider that tidal transport is one dimensional. Such additional processes are left for future study.

2.1.1. Modeling the Frictional Term

We treat the nonlinear bed stress term following the Godin (1991a, 1991b, 1999) approach, in which the frictional term, $u|u|$, is represented analytically with Chebyshev polynomials (Dronkers, 1964). The expansion is expressed as follows:

$$\frac{u|u|}{U_{(x)}^2} \approx Au' + Bu'^3 + Cu'^5 + \ldots \quad (5)$$

where $U_{(x)}$ is the maximum value of the current at point x (i.e., the sum of the amplitudes of all waves) and u' is a nondimensionalized velocity that is defined as $\frac{u}{|U_{(x)}|}$ (Doodson, 1956; Godin, 1991a, 1991b). For a three-component model with river flow, we first assume a solution of the form (see also the supporting information):

$$u' = u_0' + u_1'\cos(\omega_1 t + \phi_1) + u_2'\cos(\omega_2 t + \phi_2) + u_3'\cos(\omega_3 t + \phi_3) \quad (6)$$

where u_0', u_1', u_2', and u_3' are dimensionless velocity amplitudes, ω_1, ω_2, and $\omega_3$are frequencies, and ϕ_1, ϕ_2, and ϕ_3 are phases. We substitute equation 6 into the expansion $Au'+Bu'^3$, which results in an expansion

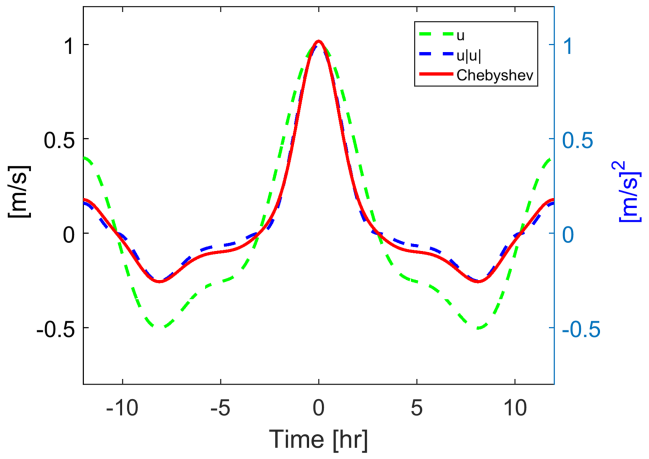

Figure 2. Example of an approximation to $u|u|$ by Chebyshev polynomials for the case of three sinusoidal components (6, 12, and 24 hr period), that is, $u_{(x,t)} = u' = 0.3\cos(\omega t) + 0.5\cos(2\omega t) + 0.2\cos(4\omega t)$, $U_{(x)} = 1$. The green line represents the velocity u (m/s). The Chebyshev approximation (red line) well represents the square of the velocity, $u|u|$ (dashed blue line).

with 24 friction terms. We then simplified by applying trigonometric identities based on the Chebyshev expansion (e.g., $\cos^3 x = \frac{1}{4}(3\cos x + \cos 3x)$; see the supporting information for a full list and the solution). The resulting expansion is a linear sum of sine waves, which includes terms with the original forcing frequencies but also additional terms that contain higher harmonics (overtides). A combination of the first (u') and third (u'^3) expansion terms is typically sufficient to obtain an accurate approximation (Godin, 1991a, 1999; Figure 2), and we use this approach here. As an example, Figure 2 shows that the combination of three tidal harmonics at the diurnal, semidiurnal, and quarter diurnal frequencies (D_1,D_2, and D_4) produces an asymmetric bed stress $u|u|$ over a tidal period (blue dashed line) and is well approximated by Chebyshev polynomials (red line). Note that $u|u|$ ((m/s)^2), which is the square of u (m/s, green line), retains the direction of stress.

For the simple case that $u_0' = u_2' = u_3' = 0$, we show in the supporting information that the semilinearization of bed stress produces a harmonic at 3 times the frequency of the original wave; for example, the standard M_2 tide wave produces an M_6 harmonic. When a mean flow is present, the M_4 harmonic is produced from M_2. When u is a function of two, three, or more sinusoidal constituents, the same expansion is used and leads to many additional overtides (harmonics) with frequencies that are sums and differences of the parent (driving) frequencies. The amount of energy transferred to higher harmonics controls the damping of constituents within a domain; the more that energy is transferred to overtides, the larger the amount of energy loss to the parent wave. As we show later, the amount of energy loss (i.e., the damping in the estuary) is strongly influenced by parameters such as depth. The nonlinear frictional term in equation 1, ($u|u|$), has been treated in a quasi-linear manner that preserves the harmonic structure of the bed stress, enabling the development of analytical or semianalytical solutions, given appropriate boundary conditions and geometry (see, e.g., Chernetsky et al., 2010).

The novel aspect of our quasi-linear analytical model is that we represent storm surge as the summation of two sinusoidal waves while representing tidal forcing with an additional sinusoid. Hence, our approach is primarily valid in locations with primarily semidiurnal or diurnal forcing (e.g., the U.S. East Coast and U. S. Gulf Coast, respectively). In section 2.1.3 we investigate the validity of representing storm surge as the sum of a primary sinusoid (Su_{Pri}) and a smaller, typically higher frequency harmonic (Su_{Sec}) (section 2.1.3). Hereafter, we employ the notation Su to denote a surge component.

2.1.2. Multisegment Approach

Our method described above is often applied by choosing a representative velocity scale that best approximates the range of velocity amplitudes found within the entire domain. A better approach, which takes into account the spatial variation in the representative velocity scale, is to split the model domain into multiple segments (Dronkers, 1964). Here, we divide up the estuary into 25 segments, where width and depth are estimated by mathematical functions (e.g., constant depth and exponential width) (e.g., Jay, 1991; Prandle & Rahman, 1980). This approach effectively divides the model domain into $N = 25$ linear problems, with $2N$ boundary conditions. At the seaward boundary, we apply three sinusoids that represent the amplitude and phase of tides and surge, while at the landward boundary we apply a no-reflection condition. A constant discharge of $u_r = 0$ is specified at the landward boundary; hence, we investigate the often-observed situation in which river flow exerts a small or negligible influence on estuarine water levels during storm events, because the flood hydrograph often occurs many days after a storm surge (e.g., Familkhalili & Talke, 2016; Orton et al., 2012; Ralston et al., 2013; Ross et al., 2017). We leave the more complex case of compound flooding and the effects of river slope to further study. The $2(N-1)$ internal boundary conditions are obtained implicitly from the solution from neighboring segments or from the applied boundary condition (outer segment). This approach allows the reflection caused by the effect of changing width on wave celerity to form in the system. To solve the system of $2N$ linear equations, we apply a Gaussian-elimination technique in which the initial value for tidal current ($u_{T(x)}$) and frictional term is estimated at each segment. Time is eliminated as an independent variable by the assumption of sinusoidal wave solutions. Substituting a

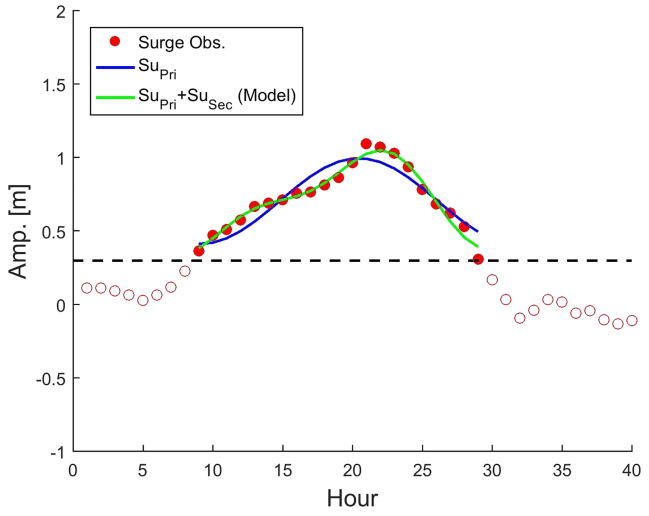

Figure 3. Decomposition of surge into different sinusoidal waves. Red circles represent the measured storm surge. The blue line is the one sine wave fit (Su_{Pri}), and the green line is a two sine wave fit and is the sum of Su_{Pri} and Su_{Sec}. The black dashed line shows the 0.3 m threshold. Here, the periods of Su_{Pri} and Su_{Sec} are 22.6 and 10.9 hr, respectively.

sinusoidal solution ($Q_{(x,t)} = Re(M_{(x)}e^{i\omega t})$; see Jay, 1991) into the wave equation (equation 4) produces a second-order ordinary differential equation that is independent of time (see equation (S11) in the supporting information). This is used, however, to represent a nonstationary situation in which amplitudes and phases may vary in time under the assumption that this variation occurs on a time scale longer than a tidal cycle. The tidal flow and wave amplitude are matched at the boundaries of N segments (Gaussian elimination). An iterative solution approach is used to match the modeled segment velocities with the estimated scale velocity in the friction term for each segment. Wave elevations ($\xi_{(x)}$) and currents ($Q_{T(x)}$) are calculated repeatedly until successive results do not vary by more than one percent.

2.1.3. Decomposing the Surge Signal

A primary assumption used in our analytical model is that storm surge can be decomposed into and represented by a limited number of sinusoidal waves. We test whether this is possible by fitting two and three sinusoidal waves with variable amplitude, frequency, and phase to measured surge waves at Lewes, DE (NOAA Station ID 8557380: 1936–2018). This station is chosen because of its location at the mouth of the Delaware River Estuary, the type of coastal plain, convergent estuary that is the focus of this study (see, e.g., DiLorenzo et al., 1993; Lee et al., 2017; Ross et al., 2017). We define surge to be the residual that is left after removing annual mean sea level and the predicted tide (using t-tide; see Leffler & Jay, 2009; Pawlowicz et al., 2002) out of the measured hourly water level. To ensure event independence, we required that surge events be at least 4 days apart. Because the tidal propagation speed is altered by the higher water levels during a storm, the actual astronomical tide arrives slightly before the predicted tide, potentially resulting in a calculated surge wave that contains a residual tide-signal (Horsburgh & Wilson, 2007). While unavoidable in this type of analysis, our choice of a coastal station minimizes this signal, since the proportional depth changes on the continental shelf are relatively small. As shown below, most of fitted surge waves are not at the D_2 frequency, suggesting that any residual tide energy does not generally dominate our surge signal.

Since surge is a nonrepeating wave, some approximations regarding the processing are unavoidable. Here, we limit ourselves to storm surge waves with amplitudes >0.5 m and fit sinusoids to the portion of the wave that exceeds a threshold of 0.3 m (see Figure 3). We find that this threshold excludes most non-storm-related water level fluctuations, while retaining sufficient data to produce a statistically significant fit. Next, a nonlinear least squares fit is used to estimate the terms in the following equation:

$$Su = C_1 + \ Su_{Pri}Cos(\omega_{Pri}t + \phi_{Pri}) + \ Su_{Sec}Cos(\omega_{Sec}t + \phi_{Sec}) \tag{7}$$

where Su is the surge amplitude, ω is the frequency of the surge wave and is inversely related to time scale T ($\omega = \frac{2\pi}{T}$), ϕ is the phase, and C_1 is an arbitrary offset that we find is ~0.45 m on average, of which 0.3 m is the arbitrary threshold. The primary and secondary waves are denoted by the *pri* and *sec* subscripts, respectively. Because seven parameters are being estimated, we require that a minimum of 10 points is fit to ensure statistical validity. A third sinusoidal wave with different frequency, phase, and amplitude was not found to significantly improve the fit to data (see the supporting information) and is not included here. Only statistically significant fits with $R^2 > 0.85$ are retained for our analysis. Of 453 surge events that were > 0.5 m from between 1936 and 2018, we are able to fit 78% with a two-wave sine model at a statistically significant level with an average root-mean-square error of 0.045 m and an average $R^2$of 0.91.

An example fit using two sinusoidal waves is shown in Figure 3. As shown, the primary sinusoid (blue line) approximates the amplitude and time scale of the surge, while the secondary sinusoid represents much of the higher frequency variability. Fitting a third sinusoid to this particular surge (not shown) results in a slightly better fit (correlation of $R^2 = 0.98$ vs. $R^2 = 0.97$ and smaller root-mean-square error of 0.03 vs. 0.04 m); however, fitting two waves is still able to approximate the time scale and amplitude of an event. We note that the fits are only valid for the time period in which surges are over the threshold value of 0.3 m.

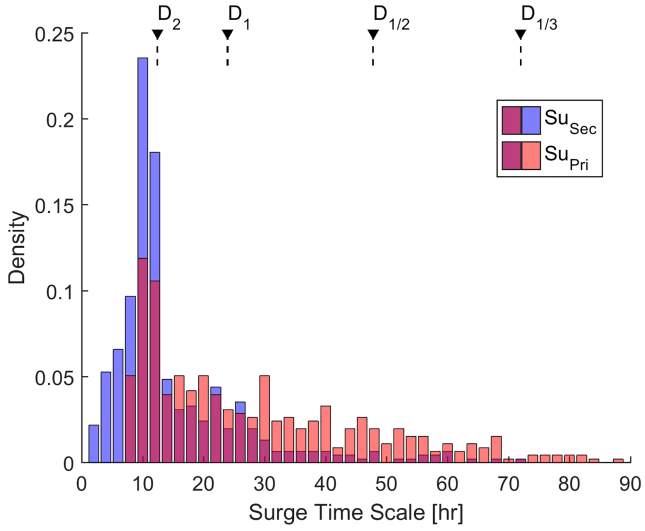

Figure 4. The probability distribution of the surge time scales $T_{pri} = \frac{2\pi}{\omega_{pri}}$, and $T_{sec} = \frac{2\pi}{\omega_{sec}}$, obtained by fitting equation 7 to hourly storm surge records from Lewes, DE (Station ID 8557380: 1936–2018). The bin width is 2 hr. The semidiurnal D_2 (2 cycles per day) to $D_{1/3}$ (one third cycle per day) time scales are labeled at the top of graph.

Using the statistically significant fits ($R^2 > 0.85$), we extract important characteristics of storm surge including its typical amplitude, time scale (wave frequency), and timing relative to tides (Figures 4 and 5). These statistics are then used to help define the parameter space that we test with our analytical model (see Table 1). Results show that the time period of the primary surge wave ranges from 8 to 89 hr (Figure 4), that is, from a time scale that is comparable to the dominant M_2 tidal period of 12.42 hr to one that is >6 times larger ($D_{1/3}$) (Figure 4). The most common time scale (the mode) is similar to the semidiurnal tide (Figure 4); approximately ~60% of surge events have periods from 1–3 times the M_2 period (average surge period is ~29.2 hr). The average period of the secondary surge wave, Su_{Sec} = 16.1 hr, is roughly one half the primary period (Figure 4). The distribution of time periods is asymmetric, however, and the median time scale for the primary and secondary surge waves (23.6 and 12.2 hr) is shorter than the average time scale. Analysis further suggests that the ratio of the primary to secondary surge amplitude ($\gamma = {Su_{Pri}}/{Su_{Sec}}$) ranges from 0.8 to 9.5, with a mean value of 2 (Figure 5a). Thus, the primary surge wave is generally larger than the secondary wave.

Similarly, the time scale of the primary sine wave is generally larger than the secondary wave, with 80% of secondary waves having a period that was between 1/2 and 1/7 the time scale of the primary wave (Figure 5b). Interestingly, the most common ratio—that is, the mode—between the primary and secondary surge period is two. Hence, the plurality of surge waves follow a pattern also seen for tides, that is, of a primary wave (e.g., M_2), which is linked to a smaller wave (M_4) of exactly twice its frequency, probably through the generation of overtides. Borrowing from the tidal literature (e.g., Chernetsky

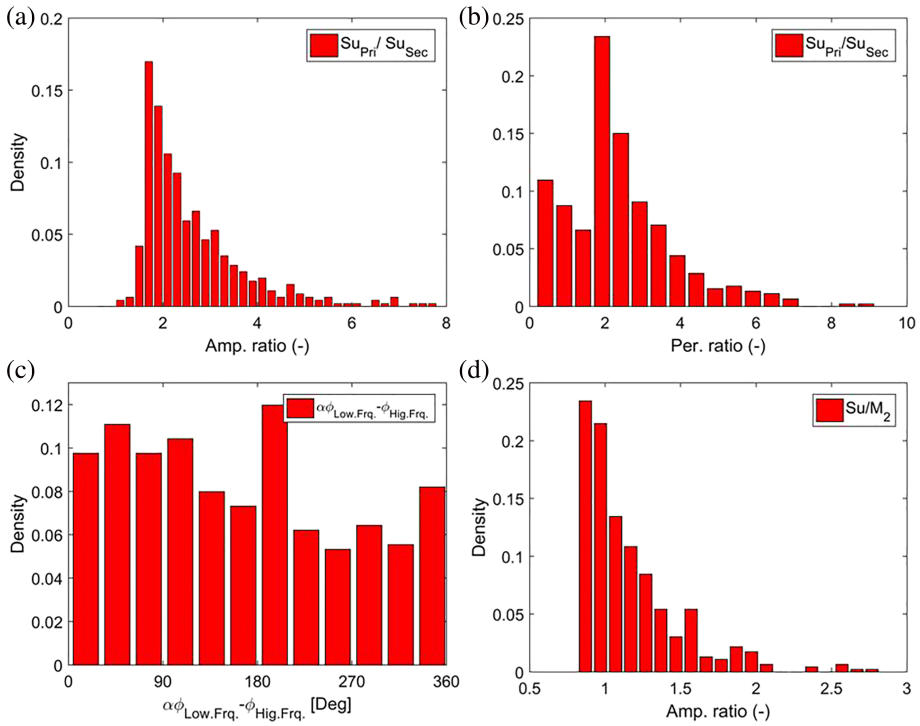

Figure 5. Probability distribution of (a) ratio of primary (Su_{Pri}) and secondary (Su_{sec}) surge wave amplitude; (b) ratio of Su_{Pri} and Su_{sec} time periods, (c) relative phase of Su_{Pri} and Su_{sec}, and (d) ratio of Su_{Pri} amplitude to M_2 amplitude. Sinusoidal surge components defined in equation 3. Data as in Figure 4.

Table 1
Parameter Space Used in Modeling, (B_0 = 5 km, L_e = 80 km, B_c = 400 m)

Depth (m)	5, 7, 10, 15, 20
Su_{Pri} *Amp. (m)*	0.5, 1, 2, 3
Su_{Pri} *Time Scale (hr)*, Su_{Sec} *Time Scale (hr)*	(12, 6) (24, 12) (48, 24) (72, 36)
Su_{Sec} *Amp. (m)*	0.25
D_2 *Time Scale (hr)*	12
D_2 *Amp. (m)*	0.5
Relative phase $\phi_{Su_{Pri}} - \phi_{Su_{Sec}}$ *(Deg)*	0 (symmetric surge) 90 (fast rise surge) 270 (slow rise surge)
Relative phase of D_2 *and* Su_{Pri} *(Deg)*	0 (surge happens at high water) 90 (surge happens at midtide) 180 (surge happens at low water)

Note. Each of the parameters is varied "one at a time", leading to hundreds of scenarios.

et al., 2010; Friedrichs & Aubrey, 1988), we therefore define a relative phase between the primary surge (frequency ω) and a secondary surge (frequency 2ω) as $(2\phi_{Su_{Pri}} - \phi_{Su_{Sec}})$. The more general formula to calculate the relative phase is $(\alpha\phi_{Lower\ freq.} - \phi_{Higherfreq.})$, where α is the ratio of $({}^{\omega_{Higherfreq.}}/_{\omega_{Lowerfreq.}})$. Therefore, Figure 5c represents the relative phase of primary and secondary surge wave by subtracting the higher frequency from the lower. As described in the tidal literature (e.g., Friedrichs & Aubrey, 1988), the value of the relative phase determines whether the wave is *slow rise* (i.e., ebb dominant with a long flood and a short ebb; largest for relative phase = 270°) or *fast rise* (short flood and long ebb; largest for relative phase = 90°). Results for surge (Figure 5c) show that the relative phase of surge waves varies between 0 and 360, that is, that storm surge can be either fast rise (0–180) or slow rise (180–360). However, close inspection shows a marked preference for relative phases between 0 and 180, which represents a symmetric wave (Figure 5c). We use this result in our analytical modeling and test the most common conditions—symmetrical, flood dominant, and ebb dominant surge waves in which the relative phase is set to 0°, 90°, and 270°, respectively, and the primary surge frequency is one half the secondary frequency.

The parameter space of our three-sinusoid model (Table 1) differs from traditional 3-tide models in several important ways: (1) the time scale of surge is not constrained to tidal bands (Figure 4) and (2) the M_2 amplitude is not necessarily the dominant amplitude. Figure 5d shows that ~60% of the surge waves in Lewes (DE) have an amplitude greater than M_2 = 0.6 m, with 5% more than twice as large. As shown in the tidal literature (e.g., Godin & Gutierrez, 1986; Jay & Flinchem, 1997), the dominant tidal constituent typically influences a smaller constituent more than vice versa; for example, M_2 produces more damping in the S_2 wave than the other way around. Hence, the ratio of surge to tide amplitude likely influences the pattern of damping and constituent attenuation within an estuary. The frequency of the wave matters as well, since lower frequency waves exhibit less damping; hence, the wide range of surge time scales becomes an important consideration (see section 3). To conclude, Figures 4 and 5 help define a parameter space that we use to model surge (Su_{Pri} and Su_{Sec}) and tides (see Table 1). We consider Su_{Pri} over a range of 12–72 hr and Su_{Sec} over a range of 6–36 hr, with the time scale of Su_{Sec} always half of Su_{Pri} . We further vary the amplitude ratio of Su_{Pri} to Su_{Sec} thru a value of 2–12 and test relative phase$\left(\phi_{Su_{Pri}} - \phi_{Su_{Sec}}\right)$ of 0°, 90°, and 270° for symmetric, fast-rise, and slow-rise surge, respectively.

2.2. Numerical Model

The multisegment model described in section 2.1 is validated against a depth-averaged idealized Delft-3D (Booij et al., 1999) numerical model that is similar to the one employed in Familkhalili and Talke (2016). The width profile in equation 3 is used, and represents a weakly convergent estuary (B_0 = 5 km, L_e = 80 km, B_c = 400 m). The domain is extended to river kilometer (Rkm) 300, to allow tides to completely damp and eliminate reflections at the upstream boundary. A Chezy coefficient of 25 $(\frac{m^{1/2}}{s})$ and a depth of 5 m is used. This parameter space corresponds to strongly dissipative and weakly convergent estuaries (Lanzoni & Seminara, 1998). This simplified geometry, while commonly used (Chernetsky et al., 2010; DiLorenzo et al., 1993; Friedrichs & Aubrey, 1994), ignores the width expansion often observed (looking upstream) in the outer portion of estuaries and the effect of large intertidal and subtidal flats. Hence, the model results are most applicable to the exponentially convergent portion of estuaries

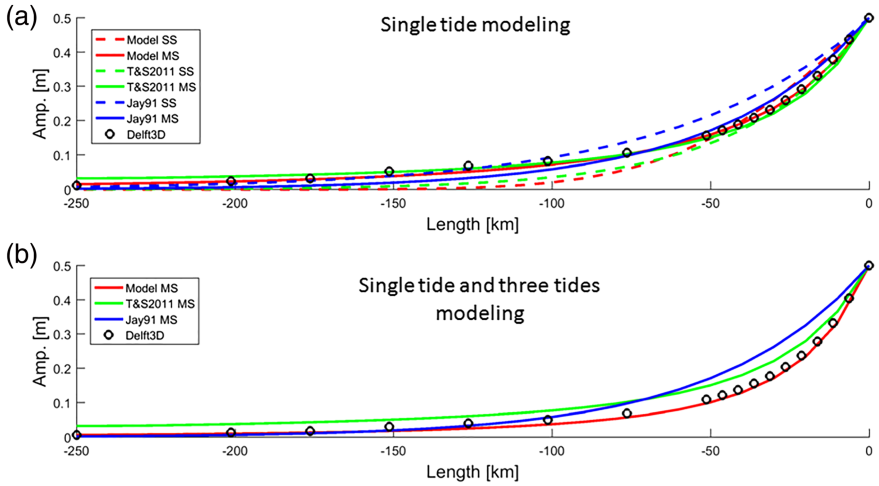

Figure 6. Evolution of dominant tidal constituent (M_2) in a 5 m deep convergent estuary for (a) single tide models (analytical and numerical models) and (b) three tides models (Model MS and Delft3D) and single tide models (T&S2011 MS and Jay91 MS) with no river flow. A U.S. East Coast estuary coordinate system in which tides move from right (the ocean/estuary boundary at Rkm 0) to left is used. SS means single segment, and MS refers to multisegment model.

upstream of an outer bay. For testing purposes, we force both the numerical and semianalytical model by the K_1, M_2, and M_3 tidal constituents at the seaward boundary and employ a spatially constant bottom friction coefficient. We run the model for 40 days to account for start-up time and include K_1, M_2, and M_3 cycles. The results of numerical modeling are analyzed using harmonic analysis (e.g., Leffler & Jay, 2009).

2.3. Model Calibration and Validation

We validate the performance of our semianalytical tide-surge model (section 2.1) against other analytical models of tides (e.g., Jay, 1991; Toffolon & Savenije, 2011) and an idealized Delft-3D numerical model (section 2.2). Because the large number of terms (24 terms) in our expansion for friction increases the probability of introducing a mathematical or programming error, we first check that our analytical tide model can reproduce the results of simpler, published one-constituent models and agrees well with the Delft-3D model. Two types of analytical model are tested—the simple single-segment model and a multisegment model in which the domain is split into 25 segments. As described in section 2.1.2, the use of multiple segments enables a spatially variable velocity scale (U_x), which improves the local validity of the Chebyshev expansion.

Using only one constituent (M_2) with no river flow, our analytical model agrees well with the Delft-3D model, the Jay (1991) approach, and the Toffolon and Savenije (2011) solution (see Figure 6a). In each case, the multisection model more closely resembles the numerical model than the single section model, demonstrating that this approach improves the observed spatial variability (Figure 6a). Overall, the one-constituent test validates our derivation of geometric and frictional effects in a one tide model but does not yet validate nonlinear interactions between terms. To validate the three-wave model, we next compare our analytical approach to the Delft-3D model with identical geometry and boundary conditions (Figure 6b).

Figure 6b shows the spatial evolution of the M_2wave in our three-wave model under forcing by the K_1, M_2, and M_3 constituents at the open ocean boundary at Rkm 0 (see solid red line; note river flow is neglected). The amplitudes of $K_1$and M_3 are made artificially large, so that the test model more closely replicates our parameter space (the M_2tide plus two sinusoids for surge); the coastal amplitudes are 0.25, 0.5, and 0.25 m for K_1, M_2, and M_3, respectively. As shown, our three-wave analytical and numerical models closely agree, particularly for the multisegment model, and validate our approach. Interestingly, the one-constituent models (Jay91 and T&S2011), replotted in Figure 6b from Figure 6a, overestimate the M_2 amplitude. Effectively, adding more constituents increases the frictional damping of M_2, resulting in a spatially variable decrease in M_2amplitude that is maximal around Rkm 50. We show below that this same process of constituent

interaction and enhanced damping will also occur when surge is approximated by a tide constituent, to a degree that is related to the relative amplitude of the surge wave and M_2.

2.4. Parameter Space

We use our validated, semianalytical, three-sinusoid model to investigate the effects of estuary depth, surge wave time scale, amplitude, and relative phase on the spatial evolution of water levels in estuaries. We apply a semidiurnal (D_2) wave with a period of 12 hr and amplitude of 0.5 m to represent typical tidal forcing (we hereafter refer to tidal bands such as D_2, rather than individual tidal constituents; this makes our analysis more general and highlights that the tidal forcing which interacts with storm surge is the sum of M_2, S_2, N_2, and many other (minor) constituents). A convergence length of 80 km is used, and the effects of river flow are neglected. The secondary surge amplitude (Su_{Sec}) of 0.25 m is held constant to model the primary to secondary surge amplitude ranges from Figure 5a. The parameters in Table 1 are varied individually, with other parameters held constant. The semianalytical solution takes ~0.25 min on a desktop computer, enabling the parameter space to be quickly tested.

The parameters in Table 1 are presented in dimensional form, for ease of interpreting results relative to real estuaries and tide/surge scenarios. However, we note that varying each of these parameters also traces out a nondimensional parameter space; in our figures we use both dimensional and nondimensional parameters, where appropriate. Independent nondimensional variables include the ratio of surge amplitude to D_2 tide ($\gamma = \frac{Amp.Su_{Pri}}{Amp.D_2}$), the ratio of Su_{Pri} time scale to D_2 period ($\Omega = \frac{Period\ \ Su_{Pri}}{Period\ \ D_2}$), and the friction scale ($\psi = \frac{C_d \xi \omega^2 L_e^3}{gh^3}$) (see the supporting information for more information). Parameter ψ suggests that increasing depth and wave time scale ($^1/_\omega$), or decreasing amplitude ξ, has a similar effect as decreasing the drag coefficient (see section 3). Other parameters that are varied include the surge/surge amplitude ratio $\left(\frac{Amp.Su_{Pri}}{Amp.Su_{Sec}}\right)$, the tide amplitude to channel depth ratio $\left(\frac{Tide\ Amp.}{Channel\ Depth}\right)$ ratio, the relative phase of storm surge (which drives the surge asymmetry), and the relative phase of surge and tide (which drives the timing of surge relative to high water/low water). For plotting purposes, we also define the following nondimensional numbers: a normalized amplitude $\left(\delta = \frac{Amp.Su_{Pri}}{Max.\ \ Surge\ Amp.}\right)$ and a dimensionless coordinate system ($L_* = x/L_e$), where L_* is normalized length.

3. Results

The parameter space described above (section 2.4) is used to investigate the amplitude of the primary surge component (Su_{Pri}) along the channel for different conditions (Table 1). This approximates the first-order behavior of the surge wave (we leave detailed analysis of the smaller secondary surge component and harmonics generated by wave interaction to future study; see the supporting information for full model and additional information). Figure 7 shows the spatial pattern of damping that occurs when the amplitude of a surge wave with a time scale of 12 hr is varied from 0.5 to 3 m (γ=1 to 6). These results reflect conditions in which the frictional interaction is likely to be largest: a symmetric surge with a phase lag of 0° relative to the D_2wave (such that the surge comes in with the flood tide and leaves with the ebb).

For the chosen parameters, the spatial progression in surge amplitude Su_{Pri} closely follows the pattern of the D_2 tide between the ocean (L_*=0) and the landward boundary (Figure 7). The *e*-folding scale for damping of surge amplitudes ranges from 0.4$L_*$to 0.25L_* with the smallest values (quickest damping) occurring for the largest amplitude wave (Figure 7b). (Note that an *e*-folding scale is the length required to decay to 1/*e* of the boundary value.) The slope of the amplitude decay ($^{d\delta}/_{dL_*}$) progressively decreases in the landward direction (Figure 7b) for all surge amplitudes, but the rate of decay remains largest (and the ratio of amplitude to the boundary amplitude is smallest) for the largest surge (γ=6). Physically, the larger velocity in a big surge event induces more damping, and the rate of surge amplitude reduction within the estuary increases for larger surge (Figure 7c). As a result, about 75% of modeled damping for 0.5 m surge occurs seaward of 0.5L_* but ~90% for the largest surge ($\gamma = 6$). As surge-induced damping increases, the relative importance of astronomic forcing on energy dissipation is reduced.

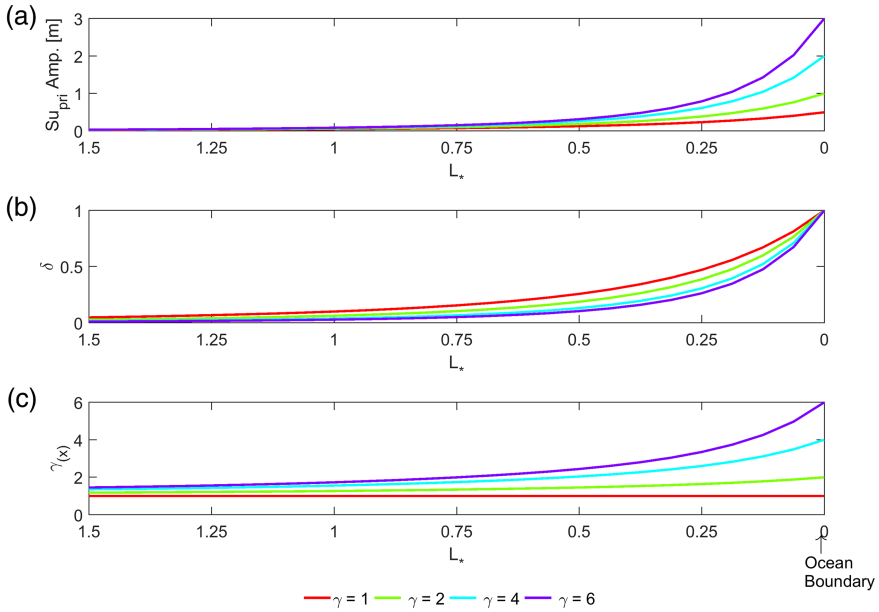

Figure 7. Spatial variation of Su_{Pri} amplitude along an idealized estuary for four different surge amplitudes at the ocean boundary (right-hand side): (a) surge amplitude (m), (b) normalized amplitude $\delta = \frac{Amp.Su_{Pri}}{Max.\ \ surge\ Amp.}$, and (c) the ratio of surge amplitudes relative over D_2 tidal amplitude, that is, $\gamma = \frac{Amp.Su_{Pri}}{Amp.\ \ D_2} = 1, 2, 4,$ and 6. The x axis is the estuary length normalized by the convergence length scale; that is, $L_* = x/L_e$.

The influence of storm surge period on nonlinear tide-surge interaction is tested by modeling a set of surge primary waves with periods from 12 hr to 72 hr (Table 1 Figure 8). As theory predicts, increasing the time scale (decreasing the frequency) of a surge wave produces a progressively lower rate of spatial decay and therefore larger upstream amplitudes (Figure 8a). For the same boundary amplitude, in other words, long-period surges produce the largest estuary and fluvial amplitudes. The largest difference in amplitude between a 12 hr (Ω=1) and 72 hr (Ω=6) surge occurs at ~0.5L_*, that is, at roughly half the e-folding length scale for geometric convergence and similar to the e-folding length scale for damping (Figure 8a). Hence, there exists in the estuary a region which is much more vulnerable to flooding from a long-period surge than a short-period surge, everything else being equal. These considerations have implications for flood hazard (see also Orton et al., 2015).

Similarly, the amplitude ratio of the primary surge component to D_2 (set equal to 1 at the ocean boundary in Figure 8) increases in the upstream direction for a slow moving storm (Figure 8b). Specifically, the 72 hr time scale surge becomes more than a factor of 4 larger than M_2 between the normalized length L_*= 0 and L_*= 1.5, while smaller time scale surges (48 and 24 hr time scale) amplify by 3.4 and 1.8 ratio relative to D_2 tide (Figure 8b). The physical reason for the slower decay of long-period surges is suggested by the friction number ψ (see Table 2) but also found by examining our solution, which shows that longer time scale surges have a lower velocity, leading to less frictional damping. For example, the ratio of Su_{Pri} velocity to D_2 velocity at the ocean boundary (L_*= 0) ranges from 1 to 0.44 for Ω =1 to 6, respectively.

Idealized surge-tide model runs also suggest that the primary surge amplitude decays less quickly in a deeper channel as it moves upstream (Figure 9), with an effect that depends on surge time scale. Hence, a 12 hr surge wave in a 5 m deep estuary under default parameters (Table 1) decays to 1/e its boundary value at $L_* = 0.35$; by contrast, a long time scale surge wave with a 72 hr time scale decays to 1/e at $L_* = 0.85$ (see dotted lines in Figures 9a and 9d). Effectively, the long time scale wave propagates twice as far. For larger depth, the e-folding scale for damping (shown by dotted line) moves upstream (to the left). The e-folding scale for a 20 m depth is 1.40 L_* and > 2.5 L_* for the 12 and 72 hr case, respectively. Therefore, fast-pulse storms remain pinned closer to the coast, while slow period waves can propagate far upstream (e.g., Ralston et al., 2019 modeled hurricane Sandy effects, a slow storm, more than 250 km from the coast). Effectively, the larger friction in a fast surge wave (ψ = 1 to 70 in Figure 9a) damps the wave more. The

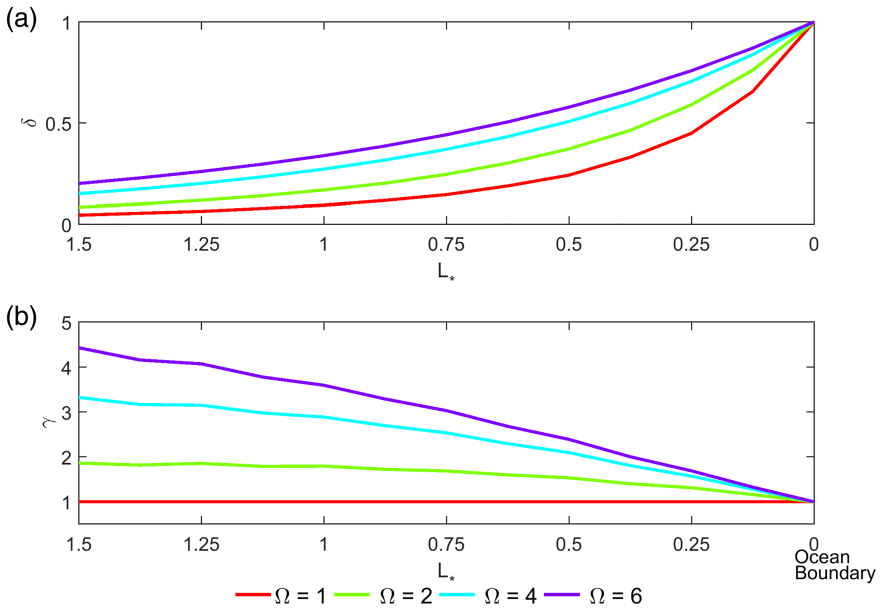

Figure 8. The influence of surge period on surge-tide decay along for four different time periods $\Omega = \frac{Period\ \ Su_{Pri}}{Period\ \ D_2} = 1, 2, 4,$ and 6, (a) normalized amplitude and (b) amplitude ratio of surge (Su_{Pri}) to D_2. The x axis is the estuary length normalized by the convergence length scale; that is, $L_* = x/L_e$

more common 24 and 48 hr times scales (see Figure 4) show an intermediate behavior (Figure 9). Since channel deepening reduces the hydraulic drag on incoming longwaves (tides and surge; effectively, a decreased friction parameter), Figure 9 is consistent with the hypothesis that both tides and storm surge can increase due to channel deepening over decadal and secular time scales (e.g., Talke et al., 2014; Winterwerp et al., 2013). Moreover, as depth increases, surge propagates further upstream. As an example, Figure 9a shows that a 12 hr surge wave with $\Omega = 1$ decays to 50% of its boundary value by $L_{*50} = 0.23$ for $\psi = 70$ (5 m depth) but at $L_{*50} = 1$ for $\psi = 1$ (20 m depth).

The increased intrusion of surge as depth is increased is shown by the contours in Figure 9, which all slant left. The amount of leftward tilt indicates the degree of sensitivity of surge to increased depth. When contours are nearly vertical, a change in depth h has little effect on surge magnitudes. Near the ocean boundary (L_*= 0), modeled storm surge (and tidal) amplitudes are little affected by channel deepening, primarily because boundary forcing is held constant and changes aggregate in the upstream direction (note that changing tidal amplitudes in an estuary can theoretically affect continental shelf or basin tides (e.g., Arbic et al., 2009; Godin, 1993); however, trends in coastal tidal amplitudes are generally much smaller than within estuaries (see review by Talke & Jay, 2020), and we neglect this factor). By contrast, the largest percentage change in amplitude is observed far upstream ($L_* > 1$) where the contours are most tilted. However, because magnitudes are small, the absolute change is small.

Figure 9 therefore shows that the increase in surge amplitude for an incremental increase in depth is a function of location. At $L_* = 0$ there is no change, since we assume that continental shelf tides are stationary. Within the estuary, the sensitivity at a given L_* to a depth change h is given by the width of the contours; a small contour width in the y direction indicates a large increase in magnitude as depth is increased. Careful examination shows that the contour spacing decreases as L_* increases from $L_* = 0$, up to a location of maximum sensitivity to h (black dashed line). Further upstream, the sensitivity to a h diminishes (in an absolute sense), given the smaller amplitudes in the upstream domain. The largest-amplitude change therefore typically occurs in the

Table 2
Nondimensional Parameter Space, Based on the Range of Dimensional Parameters in Table 1

	Minimum	Maximum
$\gamma\ (\frac{Amp.Su_{Pri}}{Amp.D_2})$	1	6
$\Omega\ \left(\frac{Period\ \ Su_{Pri}}{Period\ \ D_2}\right)$	1	6
$\delta\ \left(\frac{Amp.\ \ Su_{Pri}}{Max.Surge\ Amp.}\right)$	0	1
$\psi(\frac{C_d\xi\omega^2L_e^3}{gh^3})$	~0.03	~70

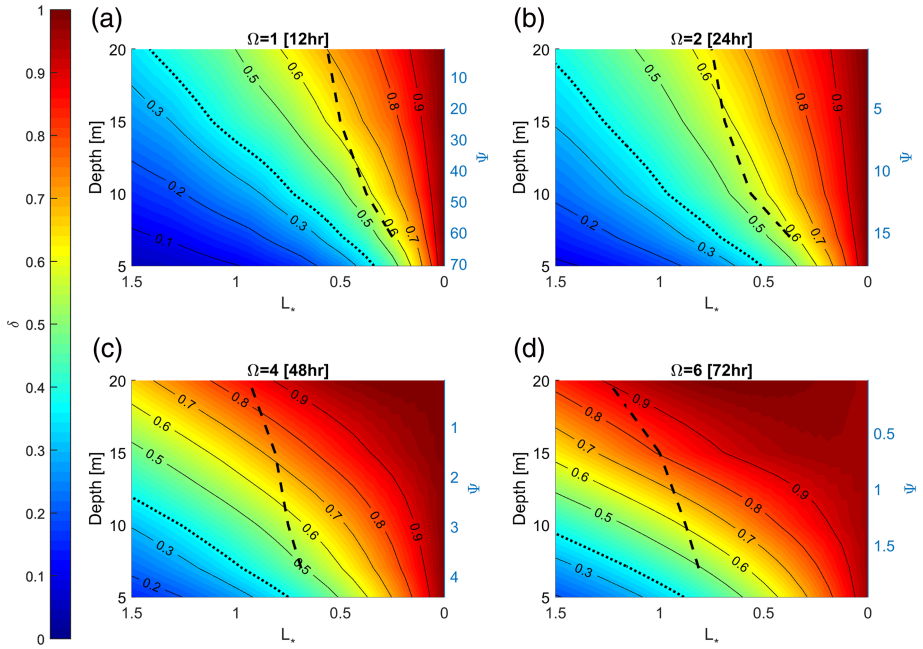

Figure 9. The influence of surge time scale and channel depth on surge-tide propagation along an idealized estuary. The color scaling represents the normalized amplitude δ and equals one at the ocean boundary, $L_* = 0$. Each plot represents a different time scale for the primary surge component, from 12 to 72 hr. For a configuration with no reflection effects, δ decreases into the estuary (left direction). The black, dashed line represents location of maximum change relative to the 5 m depth condition, and the black dotted line represents the location of the *e*-folding scale of damping, that is, the location where the primary surge wave is $1/e$ its boundary value. Note that the friction number ψ associated with each depth is plotted on the right-hand side of each plot

midestuary region. This location of maximum change typically varies between $L_* = 0.5$ and $L_* = 1$ (the convergence length scale) and moves landward as surge time scale Ω increases (see Figures 9 and 10).

Figure 10 shows that the location of maximum sensitivity to channel deepening ($L_{*max} = L_{max}/L_e$) is a strong function of depth, surge time scale, and the phasing of the surge relative to the tide. When the wave is strongly affected by friction (large ψ, i.e., small depth and small time scale), the location of maximum change occurs relatively near the coast $L_{*max} \sim 0.3$–0.6, shown by the blue coloring in Figure 10. For waves less impacted by friction (larger depth and low frequency), the location of maximum change moves far upstream, sometimes exceeding the *e*-folding length scale for width convergence (red coloring, Figure 10). Some

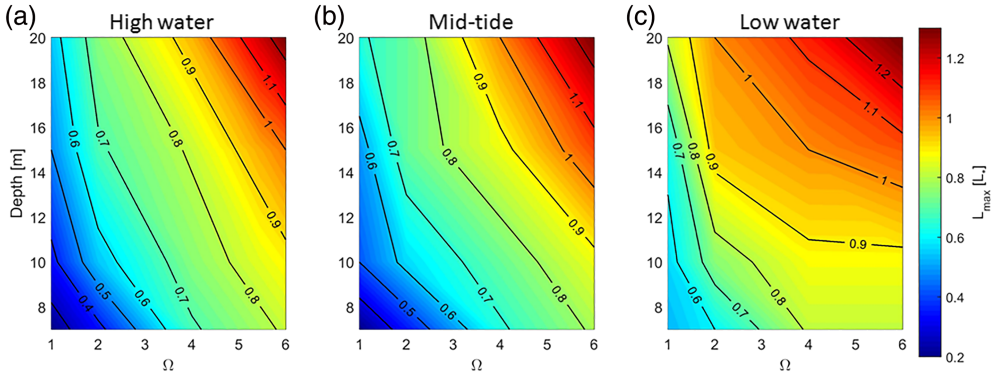

Figure 10. Location of maximum change of surge waves (L_{*max}, that occurs for depths of 7 to 20 m relative to an original depth of $h = 5$ m) for symmetric surge (relative phase of Su_{Pri} and Su_{Sec} is set to 0) at (a) high water, (b) midtide, and (c) low water as a function of channel depth and ($\Omega = \frac{Period\ \ Su_{Pri}}{Period\ \ D_2}$).

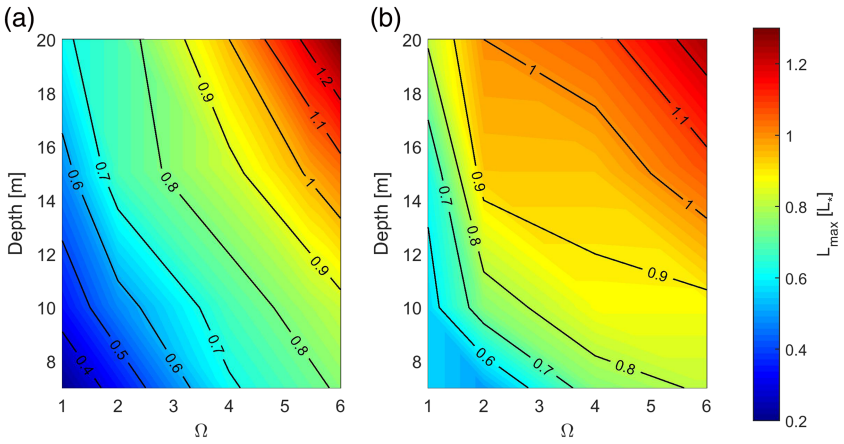

Figure 11. The effects of surge asymmetry for (a) fast-rise and (b) slow-rise surge on the location of maximum change of surge (L_{*max}) for different channel depths and ($\Omega = \frac{Period.}{Period.}\frac{Su_{Pri}}{D_2}$) with $\gamma = \frac{Amp.Su_{Pri}}{Amp.}\frac{}{D_2} = 1$ and Su_{Sec} $Amp.$of 0.25 m.

variation in L_{*max} also occurs depending on whether the peak surge occurs at the same time as high water (Figure 10a), occurs during the midtide (Figure 10b), or occurs at low water (Figure 10c). In general, L_{*max} occurs more seaward in Figure 10a than it does in Figure 10c, due to greater friction. When surge and tides come in at the same time, the total velocity (u_t+u_s) is maximal and frictional effects are larger (Figure 10a). When tide and surge velocity are more opposed, as when the ebb tide opposes the incoming surge (peak surge at low water; Figure 10c), frictional effects are less. Hence, altering tide/surge phase has similar effects as changing the friction parameter ψ.

The region of maximum sensitivity to change moves upstream as an estuary is deepened. As an example, Figure 10a shows that L_{*max} of a 12 hr surge wave (Ω =1) increases from L_{*max}~0.25 for a 7 m depth to 0.58 for a 20 m depth. As discussed in Talke and Jay (2020), the upstream movement occurs because the *e*-folding damping length scale (the length scale at which amplitudes are 1/*e* the boundary value) increases as the friction parameter ψ decreases. For a simple, tide-only model, it can be shown that the peak change occurs at approximately the damping length scale. While the inclusion of multiple wave frequencies and phases alters the actual location of L_{*max}, the general rule that L_{*max} is related to the damping length-scale holds.

The shape of the storm surge wave, as captured by the relative phase of the primary and secondary surge component, can also alter the time history of frictional effects. This also results in a different spatial pattern of surge amplitude change as an estuary is deepened. Figure 11 shows the effect of changing depth from 5 m to 7–20 m for *fast-rise* and *slow-rise* storm surge for the case that the secondary surge frequency is twice the primary (in analogy to M_2– M_4 flood and ebb-tide asymmetry, as previously discussed in section 2.1.3). In a *fast-rise* storm surge, the relative phase of Su_{Pri} and Su_{Sec} equals 90° and the incoming surge rises faster than it falls, leading to the greatest currents before peak surge; in a *slow-rise* surge, the relative phase of Su_{Pri} and $Su_{Sec} = 270°$, the rise is slower than the fall, and the greatest currents occur after peak surge. Note that, consistent with previous cases, we have kept the relative phase of M_2 and Su_{Pri} equal to 0. Results show that the location of maximum change (L_{*max}) is more variable for a fast-rise wave than a slow-rise surge wave, due to larger changes in total velocity (u_t+u_s) as a channel is deepened. Figure 11a shows that for a 12 hr, fast-rise surge ($\Omega = 1$), L_{*max} varies from ~0.35 (7 m depth) to 0.68 (20 m depth); for a slow-rise surge, L_{*max} varies from ~0.55 (7 m depth) to 0.8 (20 m depth) (Figure 11b). Essentially, as intuition might suggest, Figure 11 shows that larger velocities during the rising surge are effective at moving the location of maximum change seaward, due to larger damping. By comparison, velocities after peak surge matter less to the spatial pattern of peak surge amplitude, and therefore the spatial pattern of change.

One practical implication of Figures 10 and 11 is that channel deepening likely exerts a different effect on each storm surge, since each occurs with a different time scale and different tide and surge amplitudes and phases. Maximal effects are observed much closer to the coast on *fast* surge (small Ω) than *slow* surge (Figure 10). Since the average storm surge time scale is between Ω=2 and Ω=3 (Figure 4),

and many estuaries have changed from 5–6 m to roughly 10–12 m depth (e.g., Cape Fear Estuary; Familkhalili & Talke, 2016), there is a zone from L_{*max}~0.5 to L_{*max}~0.9 within a weakly convergent estuary (with no reflection effects), which is most prone to altered storm surge (see also Figure 11). Maximal M_2tide change occurs somewhat closer to the coast than surge, since its time period (Ω=1) is slightly less, on average.

4. Discussion and Conclusion

We have developed a conceptual numerical model and a novel analytical modeling approach to assess the effects of different storm surge types on idealized estuarine geometries, using an approach previously applied to tides. The semianalytical model for surge-tide propagation, based on a three-sinusoidal wave model, agrees well with the one-constituent analytical models of Jay (1991) and Toffolon and Savenije (2011) and is able to reproduce constituent interaction found in a 2-D numerical model. We also show that a surge modeled by two sinusoidal components provides a reasonable approximation for measured storm surges. We then use these results to estimate typical magnitudes, time scales, and phasing of surge waves (Figures 4 and 5). Future improvements might include using more realistic waveforms to model surge, applying more realistic depth and width variations and in general considering other environmental variability and atmospheric forcing, both neglected here. Nonetheless, the advantage of our relatively simple tide model is that we can use insights from the tide literature to improve our understanding of how other longwaves such as surge evolve within tidal estuaries.

We gain insights from the analytical model into the effects of estuary configuration (e.g., depth and convergence) and storm characteristics (amplitude, time scale, and relative phase) on the spatial pattern of surge damping, and how this changes as estuaries are altered. Results suggest that the largest temporal change due to anthropogenic channel deepening will occur in situations with: (a) a large surge to D_2 amplitude ratio (i.e., larger γ); (b) small time scale (high frequency) surge waves (i.e., smaller Ω), and (c) a large percentage depth change. Future sea level rise may also alter storm surge amplitudes, to an extent that our results suggest is related to the percent depth change. Recent literature suggests that tidal amplitudes in some estuaries are sensitive to sea level rise (Holleman & Stacey, 2014; Ross et al., 2017; Lee et al., 2017; Garel & Cai, 2018; see review by Talke & Jay, 2020); our results are consistent with the predictions of these studies. As shown by Ensing et al. (2015), sea level rise effects on tides can exceed dredging effects, since geometric changes caused by dredging are confined to the shipping channel but sea level rise also affects subtidal and intertidal regions. Since we apply depth changes across a constant-depth cross-section (for simplicity), rather than just in the dredged channel, our results are indicative, rather than predictive, of the types of changes that dredging or sea level rise causes in real estuaries. We note that even the extreme estimate of ~2 m sea level rise over the next century (e.g., Parris et al., 2012) is much less than historical channel deepening, which has often doubled the depth of shipping channels (e.g., Chant et al., 2018; Familkhalili & Talke, 2016). Further research is therefore needed to investigate the types of bathymetries which are most at risk to altered sea level (Talke & Jay, 2020).

Our results also suggest that weakly convergent estuaries (the parameter space studied here) have a region of enhanced sensitivity to change that is generally located around the *e*-folding length of damping for a particular wave frequency but is modified by frictional interaction with other waves (e.g., the D_2 tide), which in turn are set in part by the amplitude ratio and surge timing (phase) and asymmetry. While storm surges may respond in a variety of ways to a perturbation in depth caused by dredging or sea level rise, surge magnitudes, time scales, and relative phases have a quantifiable distribution (Figures 4 and 5). Thus, a given storm climate is likely to produce a determinable distribution of responses in any particular estuary while individuality of storm events also complicate empirical studies (see, e.g., Familkhalili, 2019; Familkhalili & Talke, 2016).

The presence of a region of maximum change of surge wave suggests that the estuarine storm surge response to deepening will vary spatially due to effects of dredging, surge time scale, sea level rise (Figure 9), the phasing of the surge relative to the tide (Figure 10), and surge asymmetry (Figure 11). Thus, future modeling studies of surge should assess spatially varying risk due to sea level rise and bathymetric change, rather than focusing on the change at a specific location (usually a specific tide gauge).

A number of future lines of inquiry remain open in the modeling framework we have developed. The effects of river flow on peak amplitudes during a storm event, particularly the changes in river slope caused by channel deepening (e.g., Jay et al., 2011; Ralston et al., 2019), form an important part of the parameter space, particularly upstream of $L_* = 1$, where river flow effects likely increase. Further, we have focused here on estuaries marked by strong damping; future work will investigate the dynamics of strongly convergent estuaries where tides can amplify or conditions in which wave reflection is important. We note also that a number of processes have been neglected, including cross-channel bathymetric effects, overland flooding, stratification effects, the Coriolis acceleration, and the effect of local wind on the surge wave. Finally, some of the approximations in the model (such as the small-amplitude approximation) may not be valid in extremely shallow systems, especially for large surge. These, and other more complex factors (such as strong variations in depth and width), are better treated with numerical models.

To conclude, this study provides insights into how tides and surge propagate and interact and how these interactions change as estuaries are altered. Understanding surge-tide interactions in estuaries has important implications for system management and flood prediction. The results presented here may help decision makers and engineers better interpret the effects of channel deepening on surge hazard and therefore help mitigate their destructive impacts. More specifically, our idealized model suggests that continued deepening of shipping channels worldwide, combined with sea level rise, can have a significant effect on storm surge amplitudes. Deeper channels typically lead to further upstream penetration of storm surge, and amplified storm surge values at some particular locations. Since effects are spatially variable and depend on storm/tide characteristics and geometry, we suggest that (a) studies of environmental impact and sea level rise effects consider an ensemble of events that well represents natural variability (e.g., Orton et al., 2016) rather than models of the "storm of record", as is often done; and (b) that entire systems be examined for their storm-surge response, not just tide gauge locations.

Acknowledgments
Funding was provided by the U.S. Army Corps of Engineers (Award W1927N-14-2-0015) and the National Science Foundation, Awards 1455350 and 1854946. The data used in this study can be obtained from NOAA's Center for Operational Oceanographic Products and Services website (https://tidesandcurrents.noaa.gov).

References

Arbic, B. K., Karsten, R. H., & Garrett, C. (2009). On tidal resonance in the global ocean and the back-effect of coastal tides upon open-ocean tides. *Atmosphere-Ocean*, *47*, 239–266.

Arns, A., Dangendorf, S., Jensen, J., Talke, S., Bender, J., & Pattiaratchi, C. (2017). Sea-level rise induced amplification of coastal protection design heights. *Scientific Reports*, *7*, 40171. https://doi.org/10.1038/srep40171

Booij, N., Ris, R. C., & Holthuijsen, L. H. (1999). A third-generation wave model for coastal regions: 1. Model description and validation. *Journal of Geophysical Research*, *104*(C4), 7649–7666. https://doi.org/10.1029/98JC02622

Buschman, F. A., Hoitink, A. J. F., Van Der Vegt, M., & Hoekstra, P. (2009). Subtidal water level variation controlled by river flow and tides. *Water Resources Research*, *45*, W10420. https://doi.org/10.1029/2009WR008167

Cai, H., Savenije, H. H. G., & Toffolon, M. (2012). A new analytical framework for assessing the effect of sea-level rise and dredging on tidal damping in estuaries. *Journal of Geophysical Research*, *117*, C09023. https://doi.org/10.1029/2012JC008000

Chant, R. J., Sommerfield, C. K., & Talke, S. A. (2018). Impact of channel deepening on tidal and 608 gravitational circulation in a highly engineered Estuarine Basin. *Estuaries and Coasts*, *41*(6), 1587–1600. https://doi.org/10.1007/s12237-018-0379-6

Chernetsky, A. S., Schuttelaars, H. M., & Talke, S. A. (2010). The effect of tidal asymmetry and temporal settling lag on sediment trapping in tidal estuaries. *Ocean Dynamics*, *60*, 1219–1241. https://doi.org/10.1007/s10236-010-0329-8

de Jonge, V. N., Schuttelaars, H. M., van Beusekom, J. E. E., Talke, S. A., & de Swart, H. E. (2014). The influence of channel deepening on estuarine turbidity levels and dynamics, as exemplified by the Ems estuary. *Estuarine, Coastal and Shelf Science*, *139*, 46–59.

DiLorenzo, J. L., Huang, P., Thatcher, M. L., & Najarian, T. O. (1993). "Dredging impacts of Delaware estuary tides." Proc. 3rd Int. Conf. Sponsored by the Waterway, Port, Coastal and Ocean Division, ASCE Estuarine and Coastal Modeling III, Oak Brook, IL, 86–104.

Divoky, D., Battalo, R., Dean, R., Collins, I., Hatheway, D., & Scheffner, N. (2005). *Storm meteorology: FEMA coastal flood hazard analysis and mapping guidelines focused study report, 31 pp*. Agency, Washington, D. C: Fed. Emerg. Manage.

Doodson A. T. (1956). Tides and storm surge in a long uniform gulf. Proceedings of the RoyalSociety of London, A237, 325-343.

Dronkers, J. J. (1964). Tidal computations in rivers and coastal waters, North-Holland, New York, 296–304.

Ensing, H., de Swart, H. E., Henk, H. M., & Schuttelaars, M. (2015). Sensitivity of tidal motion in well-mixed estuaries to cross-sectional shape, deepening, and sea level rise: An analytical study. *Ocean Dynamics*, *65*, 933–950.

Familkhalili, R., & Talke, S. (2016). The effect of channel deepening on storm surge: Case study of Wilmington, NC. *Geophysical Research Letters*, *43*, 9138–9147.

Familkhalili, Ramin, "Analytical and numerical modeling of long term changes to tides, storm surge, and total water level due to bathymetric changes and surge characteristics" (2019). Dissertations and Theses. Paper 5014. https://pdxscholar.library.pdx.edu/open_access_etds/5014

Friedrichs, C. T., & Aubrey, D. G. (1988). Nonlinear tidal distortion in shallow well-mixed estuaries: A synthesis. *Estuarine, Coastal and Shelf Science*, *26*, 521–545.

Friedrichs, C. T., & Aubrey, D. G. (1994). Tidal propagation in strongly convergent channels. *Journal of Geophysical Research*, *99*(C2), 3321–3336. https://doi.org/10.1029/93JC03219

Garel, E., & Cai, H. (2018). Effects of tidal-forcing variations on tidal properties along a narrow convergent estuary. *Coast*, *41*(7), 1924–1942. https://doi.org/10.1007/s12237-018-0410-y

Giese, B. S., & Jay, D. A. (1989). Modeling tidal energetics of the Columbia River estuary. *Estuarine, Coastal and Shelf Science*, *29*(6), 549–571. https://doi.org/10.1016/0272-7714(89)90010-3

Godin, G. (1991a). Compact approximations to the bottom friction term for the study of tides propagating in channels. *Continental Shelf Research*, *11*(7), 579–589.
Godin, G. (1991b). Frictional effects in river tides. In B. B. Parker (Ed.), *Tidal hydrodynamics* (pp. 379–402). New York: John Wiley & Sons.
Godin, G. (1993). On tidal resonance. *Continental Shelf Research*, *13*, 89–107.
Godin, G. (1999). The propagation of tides up rivers with special considerations on the upper Saint Lawrence River. *Estuarine, Coastal and Shelf Science*, *48*, 307–324.
Godin, & Gutierrez (1986). Non-linear effects in the tide of the Bay of Fundy. *Continental Shelf Research*, *5*(1986), 379–402.
Holleman, R. C., & Stacey, M. T. (2014). Coupling of sea level rise, tidal amplification and inundation. *Journal of Physical Oceanography*, *44*, 1439–1455.
Horsburgh, K. J., & Wilson, C. (2007). Tide-surge interaction and its role in the distribution of surge residuals in the North Sea. *Journal of Geophysical Research*, *112*, C08003. https://doi.org/10.1029/2006JC004033
Jay, D. A. (1991). Green's law revisited: Tidal long-wave propagation in channels with strong topography. *Journal of Geophysical Research*, *96*(C11), 20,585. https://doi.org/10.1029/91JC01633
Jay, D. A., & Flinchem, E. P. (1997). Interaction of fluctuating river flow with a barotropic tide: A test of wavelet tidal analysis methods. *Journal of Geophysical Research*, *102*, 5705–5720.
Jay, D. A., Leffler, K., & Degens, S. (2011). Long-term evolution of Columbia River tides. *ASCE Journal of Waterway, Port, Coastal, and Ocean Engineering*, *137*, 182–191. https://doi.org/10.1061/(ASCE)WW.1943-5460.0000082
Kukulka, T., & Jay, D. A. (2003). Impacts of Columbia River discharges on salmonid habitat: 2. Change in shallow-water habitat. *Journal of Geophysical Research*, *108*(C9), 3294. https://doi.org/10.1029/2003JC001829
Lanzoni, S., & Seminara, G. (1998). On tide propagation in convergent estuaries. *Journal of Geophysical Research*, *103*(30), 793–30,812.
Lee, S. B., Li, M., & Zhang, F. (2017). Impact of sea level rise on tidal range in Chesapeake and Delaware bays. *Journal of Geophysical Research: Oceans*, *122*, 3917–3938. https://doi.org/10.1002/2016JC012597
Leffler, K. E., & Jay, D. A. (2009). Enhancing tidal harmonic analysis: Robust (hybrid L1/L2) solutions. *Continental Shelf Research*. https://doi.org/10.1016/j.csr.2008.04.011
Lyddon, C., Brown, J. M., Leonardi, N., & Plater, A. J. (2018). Flood Hazard assessment for a hyper-tidal estuary as a function of tide-surge-morphology interaction. *Estuaries and Coasts*, 1–22.
Maskell, J., Horsburgh, K., Lewis, M., & Bates, P. (2013). Investigating river-surge interaction in idealised estuaries. *Journal of Coastal Research*, *30*, 248–259.
McRobie, A., Spencer, T., & Gerritsen, H. (2005). The big flood: North Sea storm surge. *Philosophical Transactions of the Royal Society, A*, *363*(1831), 1263–1270. https://doi.org/10.1098/rsta.2005.1567
Orton, P., Georgas, N., Blumberg, A., & Pullen, J. (2012). Detailed modeling of recent severe storm tides in estuaries of the New York City region. *Journal of Geophysical Research*, *117*, 1–17. https://doi.org/10.1029/2012JC008220
Orton, P., Talke, S., Jay, D., Yin, L., Blumberg, A., Georgas, N., et al. (2015). Channel Shallowing as mitigation of coastal flooding. *Journal of Marine Science and Engineering*, *3*(3), 654–673. https://doi.org/10.3390/jmse3030654
Orton, P. M., Hall, T. M., Talke, S., Blumberg, A. F., Georgas, N., & Vinogradov, S. (2016). A validated tropical-extratropical flood hazard assessment for New York Harbor. *Journal of Geophysical Research: Oceans*, *121*, 8904–8929. https://doi.org/10.1002/2016JC011679
Parker, B. B. (1991). The relative importance of the various nonlinear mechanisms in a wide range of tidal interactions. In B. B. Parker (Ed.), *Progress in tidal hydrodynamics* (pp. 237–268). John Wiley.
Parris, A., Bromirski, P., Burkett, V., Cayan, D., Culver, M., Hall, J., et al. (2012). Global Sea level rise scenarios for the US National Climate Assessment. *NOAA Tech Memo OAR*, *CPO-1*, 37.
Pawlowicz, R., Beardsley, B., & Lentz, S. (2002). Classical tidal harmonic analysis including error estimates in MATLAB using T_TIDE. *Computers and Geosciences*, *28*, 929–937.
Peng, M., Xie, L., & Pietrafesa, L. J. (2004). A numerical study of storm surge and inundation in the Croatan–Albemarle–Pamlico Estuary System. *Estuarine, Coastal and Shelf Science*, *59*(1), 121–137. https://doi.org/10.1016/j.ecss.2003.07.010
Prandle, D., & Rahman, M. (1980). Tidal response in estuaries. *Journal of Physical Oceanography*, *10*(10), 1552–1573.
Ralston, D. K., Talke, S., Geyer, W. R., Al-Zubaidi, H. A. M., & Sommerfield, C. K. (2019). Bigger tides, less flooding: Effects of dredging on barotropic dynamics in a highly modified estuary. *Journal of Geophysical Research: Oceans*, *124*, 196–211. https://doi.org/10.1029/2018JC014313
Ralston, D. K., Warner, J. C., Geyer, W. R., & Wall, G. R. (2013). Sediment transport due to extreme events: The Hudson River estuary after tropical storms Irene and Lee. *Geophysical Research Letters*. https://doi.org/10.1002/2013GL057906
Rego, J. L., & Li, C. (2010). Nonlinear terms in storm surge predictions: Effect of tide and shelf geometry with case study from Hurricane Rita. *Journal of Geophysical Research*, *115*(6), 1–19. https://doi.org/10.1029/2009JC005285
Ross, A. C., Najjar, R. G., Li, M., Lee, S. B., Zhang, F., & Liu, W. (2017). Fingerprints of sea level rise on changing tides in the Chesapeake and Delaware Bays. *Journal of Geophysical Research: Oceans*, 122. https://doi.org/10.1002/2017JC012887
Schureman, P. (1934). *Tides and currents in Hudson River* (Vol. 180). Washington, DC: United States 688 government printing office.
Shen, J., Wang, H., Sisson, M., & Gong, W. (2006). Storm tide simulation in the Chesapeake Bay using an unstructured grid model. *Estuarine, Coastal and Shelf Science*, *68*(1), 1–16. https://doi.org/10.1016/j.ecss.2005.12.018
Talke, S. A., & Jay, D. A. (2020). Changing tides: The role of natural and anthropogenic factors. *Annual Review of Marine Science*. https://doi.org/10.1146/annurev-marine-010419-010727
Talke, S. A., Orton, P., & Jay, D. A. (2014). Increasing storm tides in New York Harbor, 1844–2013. *Geophysical Research Letters*, *41*, 3149–3155. https://doi.org/10.1002/2014GL059574
Toffolon, M., & Savenije, H. H. (2011). Revisiting linearized one-dimensional tidal propagation. *Journal of Geophysical Research*, *116*, C07007. https://doi.org/10.1029/2010JC006616
van Rijn, L., Grasmeijer, B., & Perk, L. (2018). *Ocean Dynamics*, *68*(11), 1457–1479. https://doi.org/10.1007/s10236-018-1204-2
Winterwerp, J. C., Wang, Z. B., van Braeckel, A., van Holland, G., & Kösters, F. (2013). Man-induced regime shifts in small estuaries—II: A comparison of rivers. *Ocean Dynamics*, *63*, 1293–1306.
Wolf, J., & Flather, R. A. (2005). Modelling waves and surges during the 1953 storm. *Philosophical Transactions of the Royal Society, A*, *363*, 1359–1375. https://doi.org/10.1098/rsta.2005.1572
Xia, M., Xie, L., Pietrafesa, L. J., & Peng, M. (2008). A numerical study of storm surge in the Cape Fear River estuary and adjacent coast. *Journal of Coastal Research*, *24*(September 2006), 159–167. https://doi.org/10.2112/06-0795.1